Wall-to-Bed Heat Transfer in Gas–Solid Bubbling Fluidized Beds

D. J. Patil, J. Smit, M. van Sint Annaland, and J. A. M. Kuipers
Faculty of Science and Technology, Twente University, 7500 AE, Enschede, The Netherlands

DOI 10.1002/aic.10590
Published online September 8, 2005 in Wiley InterScience (www.interscience.wiley.com).

The wall-to-bed heat transfer in gas–solid fluidized beds is mainly determined by phenomena prevailing in a "thermal boundary layer " with a thickness in the order of magnitude of the size of a single particle. In this thermal boundary layer the temperature gradients are very steep and the local porosity profile near the wall strongly influences the heat-transfer rate. A two-fluid continuum model based on conservation laws for mass, momentum and thermal energy has been developed accounting for the porosity distribution near the wall. To validate the model, local instantaneous wall-to-bed heat-transfer coefficients were measured along a heated wall kept at constant temperature. The incorporation of a porosity profile by effective conductivities has remarkably improved the prediction of the heat-transfer coefficients compared against that of previous studies. The predicted local instantaneous heat-transfer coefficients are in good agreement with the experimental data for different jet velocities as well as for different particle sizes, provided that the near-wall porosity profile is accounted for. Two sets of closure equations for the solids-phase rheology (that is, the solids-phase stress tensor) have been considered: the constant viscosity model (CVM) and the kinetic theory of granular flow (KTGF). For lower bed heights both models give good predictions of the wall-to-bed heat-transfer coefficients, but the KTGF predictions at higher bed heights agree better with the experimental data than the predictions by the CVM as the result of a better description of the passage of the bubble along the wall. The influence of an additional kinetic contribution to the effective solids-phase thermal conductivity arising from the fluctuating solids velocity was studied with the KTGF closures. Because of a large overprediction of the kinetic solids-phase thermal conductivity the wall-to-bed heat-transfer coefficients are largely overestimated when accounting for this additional contribution to the effective solids-phase thermal conductivity. © 2005 American Institute of Chemical Engineers *AIChE J,* 52: 58–74, 2006
Keywords: heat transfer, fluidized beds, continuum modeling, kinetic theory of granular flow, porosity profile

Introduction

Fluidized beds find widespread application in highly thermal processes because of their excellent heat-transfer properties. In many of these applications heat transfer between the bed and an immersed surface is involved. Unfortunately, it is still very difficult to predict the values for the local heat-transfer coefficients with confidence. Many empirical correlations for the wall-to-bed heat-transfer coefficient have been published in the literature, but the use of these expressions is limited to the experimental conditions on which they are based. From a scientific perspective, these empirical correlations are less attractive because they generally do not provide a fundamental understanding of the prevailing transport mechanisms. With

Correspondence concerning this article should be addressed to M. van Sint Annaland at M.vanSintAnnaland@tnw.utwente.nl

increasing computational power, numerical simulation has become an indispensable tool to study fluid dynamics and heat transfer in multiphase flows. In recent years, several studies[1,2] have been carried out to model wall-to-bed heat transfer in bubbling fluidized beds. However, the heat-transfer coefficients predicted by their models were much too high compared to experimentally observed heat-transfer coefficients.

Although in most industrial processes, tube-to-bed heat transfer is involved, a simplified geometry is considered in this work to better study the fundamental transfer processes and to ease the experimental work for validation of the model predictions. In this work the heat transfer from a fluidized bed with a flat wall is studied. A two-dimensional fluidized bed operated with a (pulsating) jet—for which the bubble dynamics can be described sufficiently accurately with existing Eulerian models[3]—will be studied and the influence of bubble dynamics on the wall-to-bed heat transfer will be investigated both theoretically and experimentally. A (pulsating) jet is used to achieve controlled, nonchaotic heat-transfer behavior in both the measurements and the simulations to facilitate the comparison of the experimental and simulation results to study the fundamental heat-transfer processes in depth, among which is the effect of the wake of the gas bubble.

Previous studies[1,2] have shown that the thermal boundary layer thickness is of the size of a particle diameter. Therefore, the variation of important parameters in this region has a major influence on the prediction of heat-transfer characteristics. Near the wall, at the scale of a particle diameter, the local porosities differ from the bulk porosities and depend on the particle diameter and the distance from the wall. However, Eulerian models describe the near-wall porosity equal to the bulk porosity. Therefore, it is important to apply a "subgrid model " for the description of the influence of the porosity near the wall when solving the thermal energy balance. In this work, a computational study using a subgrid model for the description of the porosity distribution near the wall has been carried out to investigate the fundamental mechanisms of the wall-to-bed heat transfer and to elucidate the influence of hydrodynamic parameters on the heat-transfer characteristics. The model predictions were validated with dedicated experimental measurements for which a special experimental setup has been constructed.

In this article, first the experimental setup is shortly described, with which the local instantaneous wall-to-bed heat-transfer coefficients were measured in a pseudo two-dimensional bubbling fluidized bed operated with a jet near the wall. Subsequently, the *two-fluid model* and its closure equations, which include the porosity distribution near the wall and the effective conductivities, are described. To understand the mechanisms of the wall-to-bed heat transfer, the predicted heat-transfer coefficients along the heated wall during the passage of a bubble were compared with experimental measurements. The influence of the jet velocity and particle diameter on the heat-transfer coefficient was also investigated. Furthermore, the influence of the kinetic contribution in the effective solids-phase conductivity was analyzed using the two-fluid model with closures for the solids-phase rheology derived from the kinetic theory of granular flow.

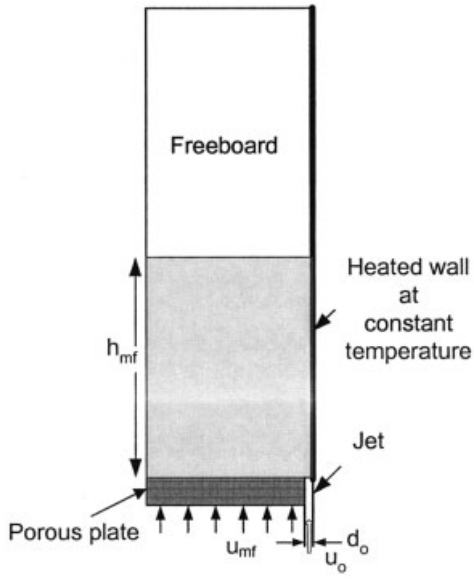

Figure 1. Experimental setup.

Experimental Setup

The principal objective of the experimental study is to provide reliable data for a thorough validation of the model predictions. In many industrial applications involving heat transfer in fluidized beds, heat-transfer tubes are immersed in the fluidized bed. However, to facilitate our study, a simpler bed geometry has been selected: a pseudo two-dimensional fluidized bed ($0.2925 \times 1.0 \times 0.015$ m) with a heated wall, where bubbles were introduced into the bed by a jet positioned just at the heated wall (see Figure 1).

The primary fluidizing gas was uniformly distributed using a porous-plate gas distributor and an inlet section that was filled with glass beads of 3 mm diameter to further promote a homogeneous gas flow distribution. The secondary fluidizing gas was injected in the fluidized bed through a jet, which was placed near the heated wall of the fluidized bed. The heated wall was made of copper and kept at a temperature higher than that of the fluidized bed using heaters placed inside the wall. The temperature of the copper strip was measured with thermocouples at different places and kept uniform (at 333 K) using PID (proportional–integral–derivative) controllers. The local instantaneous heat flux from the copper strip to the bed was measured with a commercial heat-flux sensor (Micro-Foil heat-flow sensor, No. 20450-1; RdF Corp., Hudson, NH). Four sensors were mounted onto the copper strip to measure the heat flux at 0.026, 0.092, 0.175, and 0.259 m above the bottom of the distributor plate. The measuring principle of the sensor is based on the measurement of the temperature drop over a thermal barrier by the corresponding voltage difference, which can be correlated to a heat flux. This sensor is of the thermocouple type, consisting of Chromel and Alumel strips in series (to enhance the signal) with the soldering points on each side of a thin, plastic foil with a low thermal conductivity (see Figure 2).

The sensor has a measuring area of 1.5×1.5 mm and a total thickness of 0.12 mm. It is coated with polyimide (thickness 0.010 mm) to protect the sensor. The response time of the sensor is 20 ms for a 62% step response. The heat-transfer coefficient is calculated by

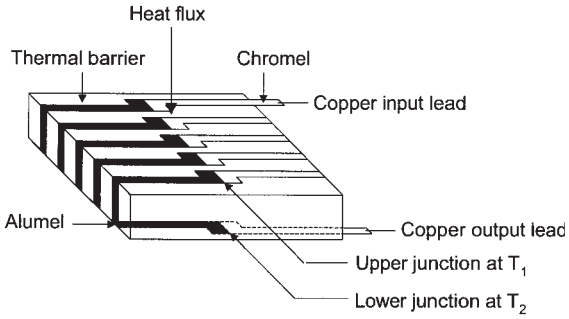

Figure 2. Overview of the heat flux sensor.

$$\alpha = \frac{J_h}{T_w - T_{bed}} = \frac{f_{corr}V}{S(T_w - T_{bed})} \tag{1}$$

where T_w and T_{bed} are the wall and bed temperature (K), respectively; J_h is the heat flux (W/m^2); f_{corr} is a temperature-dependent correction factor (dependent on the temperature at the back of the sensor, in this case the wall temperature) supplied by the manufacturer for each sensor; V is the voltage drop over the sensor (V); and S is the sensor sensitivity ($\sim 6.0 \times 10^{-9}$ Vm^2/W, which is also supplied by the manufacturer for each sensor). The time constant of the heat flux sensors as reported by the RdF Corp. is 0.02 s. The output signal of the sensors was recorded by a data-acquisition card (PCL-818HG and PCLD-8115 wiring terminal board; Advantech Automation, Cincinnati, OH), with a maximal sampling frequency of 200 Hz. The error in the measurement of the heat-transfer coefficient was typically <5 W m^{-2} K^{-1}.

The bed was filled to a height of 0.35 m with glass beads of 280 or 460 μm diameter and was kept at minimum fluidization conditions by primary fluidizing air. At zero time, gas was passed through the jet with a velocity much higher than the minimum fluidization velocity. This causes the formation of a gas bubble, which travels along the wall, which is kept at a constant temperature. At the same time, the heat flux was measured with the sensors. These experiments were carried out with different jet velocities as well as with particles of different size to quantitatively measure the effect of bubble passages along the heated wall on the local heat-transfer rate. Experiments were carried out with a pulsating jet, using a pulse length of 0.25 s and a pulse interval of 0.25 s, and with a continuous jet operation.

Two-Fluid Model

A two-fluid model is used to describe the wall-to-bed heat transfer and is based on conservation equations for mass, momentum, and thermal energy for both phases, which are both considered as interacting interpenetrating continua (Euler–Euler model). The model equations are summarized in Table 1. The viscous dissipation and work terms are small when compared to the other terms in the heat balance (accumulation, conduction, convection, and interphase transfer) and therefore these terms were neglected. The interphase momentum transfer coefficient is described by the equations of Ergun[4] and Wen and Yu,[5] depending on the local porosity (see Table 2). The gas phase is assumed incompressible and Newtonian behavior is assumed for the viscous stresses generated.

The two-fluid model requires constitutive equations to describe the rheology of the solids phase, that is, the solids-phase viscosity and the solids-phase pressure gradient, for which two models have been used: the *constant viscosity model* (CVM) and the *kinetic theory of granular flow* (KTGF). In the CVM the solids-phase pressure was defined only as a function of the porosity of local solids by empirical correlations and the solids-phase viscosity was assumed constant.[1,6] The KTGF derives closure equations for the internal momentum transfer in the particulate phase using a fundamental description of the transport mechanisms in an ensemble of particles.

As a result of shearing of the particulate phase in a fluidized bed, particles collide—resulting in a random granular motion. This particle velocity fluctuation generates an effective pressure in the particulate phase, together with an effective viscosity that resists shearing of the particle assembly. Associated with the random motion of the particles, a granular temperature Θ_s can be defined as

$$\frac{3}{2}\Theta_s = \frac{1}{2}\overline{\boldsymbol{C}_s \cdot \boldsymbol{C}_s}$$

where $\boldsymbol{C}_s$ is the random fluctuating velocity of the particulate phase. Modeling of the collisional and kinetic transport mech-

Table 1. Two-Fluid Model Equations

Continuity equations

Gas phase

$$\frac{\partial(\varepsilon_f\rho_f)}{\partial t} + \nabla\cdot(\varepsilon_f\rho_f\bar{\boldsymbol{u}}) = 0 \tag{21}$$

Solids phase

$$\frac{\partial(\varepsilon_s\rho_s)}{\partial t} + \nabla\cdot(\varepsilon_s\rho_s\bar{\boldsymbol{v}}) = 0 \tag{22}$$

Momentum equations

Gas phase

$$\frac{\partial(\varepsilon_f\rho_f\bar{\boldsymbol{u}})}{\partial t} + \nabla\cdot(\varepsilon_f\rho_f\bar{\boldsymbol{u}}\bar{\boldsymbol{u}}) = -\varepsilon_f\nabla p - \beta(\bar{\boldsymbol{u}} - \bar{\boldsymbol{v}}) - (\nabla\cdot\varepsilon_f\boldsymbol{\tau}_f) + \varepsilon_f\rho_f\boldsymbol{g} \tag{23}$$

Solids phase

$$\frac{\partial(\varepsilon_s\rho_s\bar{\boldsymbol{v}})}{\partial t} + \nabla\cdot(\varepsilon_s\rho_s\bar{\boldsymbol{v}}\bar{\boldsymbol{v}}) = -\varepsilon_s\nabla p + \beta(\bar{\boldsymbol{u}} - \bar{\boldsymbol{v}}) - (\nabla\cdot\varepsilon_s\boldsymbol{\tau}_s) - \nabla p_s + \varepsilon_s\rho_s\boldsymbol{g} \tag{24}$$

Thermal energy balances

Gas phase

$$\frac{\partial(\varepsilon_f\rho_f H_f)}{\partial t} + \nabla\cdot(\varepsilon_f\rho_f\bar{\boldsymbol{u}}H_f) = \nabla\cdot\varepsilon_f k_f^{eff}\nabla T_f - \alpha(T_f - T_s) \tag{25}$$

Solids phase

$$\frac{\partial(\varepsilon_s\rho_s H_s)}{\partial t} + \nabla\cdot(\varepsilon_s\rho_s\bar{\boldsymbol{v}}H_s) = \nabla\cdot\varepsilon_s k_s^{eff}\nabla T_s + \alpha(T_f - T_s) \tag{26}$$

Table 2. Constitutive Equations for the Interphase Momentum Transfer

Interphase momentum transfer

For $\varepsilon_f < 0.8$

$$\beta = 150\frac{(1-\varepsilon_f)^2}{\varepsilon_f}\frac{\mu_f}{(\phi_s d_p)^2} + 1.75\frac{\rho_f}{(\phi_s d_p)}|\bar{\boldsymbol{u}} - \bar{\boldsymbol{v}}| \qquad C_d = \frac{24}{\mathrm{Re}_p}[1 + 0.15(\mathrm{Re}_p)^{0.687}] \quad \mathrm{Re}_p < 1000$$

$$C_d = 0.44 \quad \mathrm{Re}_p > 1000$$

For $\varepsilon_f > 0.8$

$$\beta = \frac{3}{4}\mathrm{C_d}\frac{\varepsilon_\mathrm{f}(1-\varepsilon_\mathrm{f})}{(\phi_\mathrm{s}\mathrm{d_p})}\rho_\mathrm{f}|\bar{\boldsymbol{u}} - \bar{\boldsymbol{v}}|\varepsilon_f^{-2.65} \qquad \text{where } \mathrm{Re}_p = \frac{\varepsilon\rho_f|\bar{\boldsymbol{u}} - \bar{\boldsymbol{v}}|d_p}{\mu_f}$$

anisms for the momentum and fluctuating kinetic energy of the particles[7] yields a description of the momentum transport properties as a function of the granular temperature and an additional transport equation for the kinetic energy of the random motion of the particles describing the granular temperature distribution. The transport equation and all the constitutive equations of the KTGF model are listed in Table 3. For very dense regions, the additional contribution to the momentum transfer in solids phase, resulting from long-term and multiparticle contact and deformations, was accounted for using the frictional stress model proposed by Srivastava and Sundaresan.[8]

The two-fluid model based on the KTGF assumed that the

Table 3. Constitutive Equations Based on the Solids-Phase Rheology

Constant Viscosity Model (CVM)

Solids phase pressure

$\nabla p_s(\varepsilon_f) = G(\varepsilon_f)\nabla\varepsilon_f$

$G(\varepsilon_f) = G_0 e^{-c(\varepsilon_f - \varepsilon_f^*)}$

where $G_0 = 1.0$, $c = 100$, and $\varepsilon_f^* = 0.45$[25]

Solids phase viscosity

$\mu_s = 1.0\ \mathrm{Pa}\cdot\mathrm{s}$[26,27]

Kinetic Theory of Granular Flow (KTGF)

Transport equation for the granular energy

$$\frac{3}{2}\left\{\frac{\partial}{\partial t}(\varepsilon_s\rho_s\Theta_s) + \nabla\cdot(\varepsilon_s\rho_s\Theta_s\bar{\boldsymbol{v}})\right\} = -(p_s^{kc}\bar{\bar{I}} + \varepsilon_s\boldsymbol{\tau}_s^{kc}):\nabla\bar{\boldsymbol{v}} + \nabla\cdot\bar{\boldsymbol{q}}_s - \gamma - 3\beta\Theta_s$$

Radial distribution function

$$g_0 = \frac{1 + 2.5\varepsilon_s + 4.5904\varepsilon_s^2 + 4.515439\varepsilon_s^3}{\left[1 - \left(\frac{\varepsilon_s}{\varepsilon_s^{\max}}\right)^3\right]^{0.67802}}$$

Solids phase pressure

$$p_s^{kc} = \varepsilon_s\rho_s\Theta_s + 2(1+e)\varepsilon_s^2 g_0\rho_s\Theta_s$$

Solids phase stress-tensor

$$\boldsymbol{\tau}_s^{kc} = -\left\{\left(\lambda_s - \frac{2}{3}\mu_s\right)(\nabla\cdot\bar{\boldsymbol{v}})\bar{\bar{I}} + \mu_s[(\nabla\bar{\boldsymbol{v}}) + (\nabla\bar{\boldsymbol{v}})^T]\right\}$$

Energy flux of solid phase fluctuations

$$\bar{\boldsymbol{q}}_s = \kappa_s\nabla\Theta_s$$

Solids phase shear viscosity

$$\mu_s^{kc} = \frac{4}{5}\rho_s d_p g_0(1+e)\left(\frac{\Theta_s}{\pi}\right)^{1/2} + 1.01600\frac{5}{16}\frac{m}{d_p^2}\left(\frac{\Theta_s}{\pi}\right)^{1/2}\frac{\left[1 + \frac{4}{5}(1+e)\varepsilon_s g_0\right]\left(1 + \frac{8}{5}\varepsilon_s g_0\right)}{\varepsilon_s g_0}$$

$$\kappa_s = 2\varepsilon_s\rho_s d_p g_0(1+e)\left(\frac{\Theta_s}{\pi}\right)^{1/2} + 1.02513\frac{75}{64}\frac{m}{d_p^2}\rho_s d_p\left(\frac{\Theta_s}{\pi}\right)^{1/2}\frac{\left[1 + \frac{6}{5}(1+e)\varepsilon_s g_0\right]\left(1 + \frac{12}{5}\varepsilon_s g_0\right)}{\varepsilon_s g_0}$$

Solids phase bulk viscosity

$$\lambda_s = \frac{4}{3}\rho_s d_p g_0(1+e)\left(\frac{\Theta_s}{\pi}\right)^{1/2}$$

Dissipation due to inelastic collisions

$$\gamma = 3(1-e^2)\varepsilon_s^2\rho_s g_0\Theta_p\left[\frac{4}{d_p}\left(\frac{\Theta_s}{\pi}\right)^{1/2} - \nabla\cdot\bar{\boldsymbol{v}}\right]$$

Frictional stress model[8]

$$p_s^f = p_c(\varepsilon_s) \quad \text{and} \quad \mu_s^f = \frac{p_c(\varepsilon_s)\sqrt{2}\sin\phi}{2\varepsilon_s\sqrt{\bar{\bar{D}}_{ij}:\bar{\bar{D}}_{ij} + \Theta_s/d_p^2}}$$

$$\text{where } p_c(\varepsilon_s) = \begin{cases} F\dfrac{(\varepsilon_s - \varepsilon_{s,\min})^r}{(\varepsilon_{s,\max} - \varepsilon_s)^s} & \varepsilon_s > \varepsilon_{s,\min} \\ 0 & \varepsilon_s \le \varepsilon_{s,\min} \end{cases} \qquad \bar{\bar{D}}_{ij}:\bar{\bar{D}}_{ij} = \left\{\frac{1}{2}[(\nabla\bar{\boldsymbol{v}}) + (\nabla\bar{\boldsymbol{v}})^T] - \frac{1}{3}\nabla\cdot\bar{\boldsymbol{v}}\bar{\bar{I}}\right\}$$

where $F = 0.5$, $r = 2.0$, $s = 3.0$[28]

particulate phase stress tensor is the sum of the kinetic and collisional stress tensor and the frictional stress tensor, where each contribution is evaluated as if it acted separately. Thus, the solids-phase pressure and solids-phase shear viscosity are expressed as

$$p_s = p_s^{kc} + p_s^f \tag{2}$$

and

$$\mu_s = \mu_s^{kc} + \mu_s^f \tag{3}$$

Here, the superscript *kc* refers to the kinetic and collisional contribution and *f* refers to the frictional contribution. In their frictional stress model Srivastava and Sundaresan[8] took into account the argument that even in a purely quasi-static flow fluctuations exist in the strain rate associated with the formation of a shear layer and that these fluctuations will decrease the shear stress in the particle assembly. The authors suggested an ad hoc modification, which recognizes the effect of strain rate fluctuations in an approximate manner. These closure equations are also summarized in Table 3.

Constitutive Equations for the Thermal Energy Balance

Interphase heat transfer

The volumetric interfacial heat-transfer coefficient is the product of the specific surface area and the interfacial heat-transfer coefficient, which for spherical particles is given by

$$\alpha = \frac{6\varepsilon_s}{d_p}\,\alpha_p \tag{4}$$

The interphase heat-transfer coefficient was described with the empirical relation proposed by Gunn[9]

$$\mathrm{Nu}_p = (7 - 10\varepsilon_f + 5\varepsilon_f^2)[1 + 0.7(\mathrm{Re}_p)^{0.2}(\mathrm{Pr})^{1/3}] + (1.33 - 2.40\varepsilon_f + 1.20\varepsilon_f^2)(\mathrm{Re}_p)^{0.2}(\mathrm{Pr})^{1/3} \tag{5}$$

where

$$\mathrm{Nu}_p = \frac{\alpha_p d_p}{k_f} \qquad \mathrm{Re}_p = \frac{\varepsilon_f \rho_f |\bar{u} - \bar{v}|}{\mu_f} \qquad \text{and} \qquad \mathrm{Pr} = \frac{\mu_f C p_f}{k_f}$$

Effective conductivities of the gas and solids phases

The thermal conductivity of the particulate phase differs from the particle material depending on the contacts of the particles in the fluidized bed. Based on the arrangement in sphere packing in a packed bed, Zehner and Schlünder[10] described the thermal conductivity of the bulk of the packed bed as a function of the thermal properties of the gas, particle material, and void fraction. For a mathematical description of the heat-transfer rate in the two-fluid continuum model it is necessary to separate the overall bulk thermal conductivity into a thermal conductivity of the gas phase and the solids phase separately. This has been suggested by Syamlal and Gidaspow[11] and later adapted by Kuipers et al.[1] For the gas phase, the effective thermal conductivity is given by

$$k_f^{eff} = \left(\frac{1 - \sqrt{\varepsilon_s}}{\varepsilon_f}\right) k_f \tag{6}$$

From the approach proposed by Natarajan and Hunt,[12] the effective thermal conductivity of the solids phase can be expressed as a sum of the molecular conductivity inside the solid particles and the contribution arising from the streaming of the particles, referred to as the kinetic conductivity

$$k_s^{eff} = k_s^{mol} + k_s^{kin} \tag{7}$$

The molecular conductivity can be expressed as

$$k_s^{mol} = \frac{1}{\sqrt{\varepsilon_s}}\, k_f[\omega A + (1 - \omega)\Gamma] \tag{8}$$

where

$$\Gamma = \frac{2}{\left(1 - \frac{B}{A}\right)}\left[\frac{(A-1)}{\left(1 - \frac{B}{A}\right)^2}\frac{B}{A}\ln\left(\frac{A}{B}\right) - \frac{(B-1)}{\left(1 - \frac{B}{A}\right)} - \frac{(B+1)}{2}\right]$$

and for spherical particles

$$A = \frac{k_s}{k_f} \qquad B = 1.25\left(\frac{\varepsilon_s}{\varepsilon_g}\right)^{10/9} \qquad \text{and} \qquad \omega = 7.26 \times 10^{-3}$$

where ω represents the ratio of the particle contact area to the total particle surface area.

The streaming or kinetic solids thermal conductivity is the rate of thermal energy transported as the result of the fluctuating motion of the particles. Schmidt and Renz[2] used a model introduced by Hunt[13] to describe the effective solids-phase thermal conductivity as a function of the granular temperature, that is, as a function of the kinetic energy of random particle fluctuations. Assuming a Maxwellian particle velocity distribution function (first-order approximation) to derive an expression for the mean free path of the particles in a two-dimensional system, Hunt derived the following equation for the kinetic solids-phase thermal conductivity

$$k_s^{kin} = \rho_s C_{p,s} d_p \sqrt{\Theta_s}\,\frac{\pi^{3/2}}{32 g_0} \tag{9}$$

An expression for the kinetic contribution to the solids-phase thermal conductivity can also be derived by an alternative approach in which the amount of energy carried away from the wall is equivalent to the energy transported by diffusion of particles arising from their random motion. The expression for self-diffusion given by Chapman and Cowling[14] for rigid elastic spheres of diameter d_p is given by

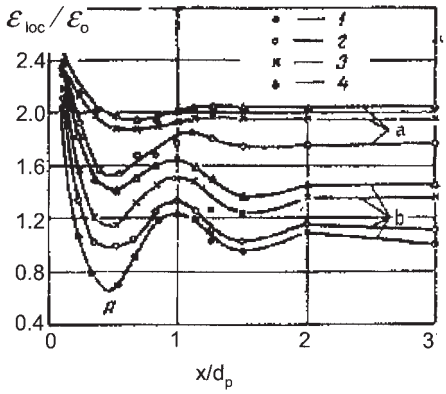

Figure 3. Near-wall porosity distribution (relative to the bulk porosity of a packed bed) for spherical polystyrene particles as a function of the relative distance to (a) an immersed surface and (b) a wall at different fluidization velocities presented by Korolev et al.[15]

1, 2, 3, and 4 correspond to u/u_{mf} = 1, 2, 4, and 8, respectively.

$$[D_{11}]_1 = \frac{d_p}{16\varepsilon_s}(\pi\Theta_s)^{1/2} \tag{10}$$

Therefore, the kinetic solids-phase thermal conductivity can be written as

$$k_s^{kin} = \varepsilon_s\rho_s C_{p_s}[D_{11}]_1 = \rho_s C_{p_s} d_p \sqrt{\Theta_s}\,\frac{\pi^{1/2}}{16} \tag{11}$$

The expression for the kinetic contribution of the solids-phase thermal conductivity obtained from the approach of particle diffusion is very similar to the expression proposed by Hunt,[13] realizing that the radial distribution function approaches unity when the solids fraction decreases to zero at the wall. The influence of k_s^{kin} on the heat-transfer characteristics is studied with the two-fluid model using the KTGF closures.

Usually, the effective conductivities appearing in the thermal energy equations are computed on the basis of the bulk porosity.[1] However, near the wall, at the scale of a single particle, the local porosities differ from the bulk porosities and depend on the particle diameter and the distance from the wall. The porosity distribution near the wall (explained in the next section) should be taken into account for the accumulation and transport of the thermal energy, ignored in previous studies on modeling the heat transfer in fluidized beds. It is not straightforward to take the porosity distribution into account in the accumulation of thermal energy, and thus it is accounted for only in the effective thermal conductivities.

Porosity distribution near the wall

Korolev et al.[15] measured the (average) local porosity in a fluidized bed near a surface. In Figure 3 the measured local porosity ε_{loc} relative to the bulk porosity ε_0 for packed beds is plotted as a function of the relative distance to the surface x/d_p for both a wall and an immersed surface and for different fluidization velocities, showing that the local porosity for both the wall and the immersed surface is dependent on the fluidization velocity. The measured local porosity distribution near a wall is very similar to that of a packed bed at low fluidization velocities, although for the immersed surface, they found that the variations in the porosity distribution are attenuated to a much greater degree. Kubie and Broughton[16] proposed a correlation to describe the local near-wall porosity profile for high fluidization velocities as

$$\varepsilon_f = 1 - 3(1-\varepsilon_f^{bulk})\left[\frac{x}{d_p} - \frac{2}{3}\left(\frac{x}{d_p}\right)^2\right] \quad \text{for} \quad 0 \le \frac{x}{d_p} \le 1$$
$$\varepsilon_f = \varepsilon_f^{bulk} \quad \text{for} \quad \frac{x}{d_p} \ge 1 \tag{12}$$

However, the local porosity distribution described by this correlation does not agree well with the experimental data by Korolev et al.[15] for different bulk porosities. For a packed bed with flat walls, Benenati and Brosilow[17] and Korolev et al.[15] measured the porosity distribution, fitted by Martin,[18] with

$$\varepsilon_f = \varepsilon_f^{\min} + (1-\varepsilon_f^{\min})\left(\frac{2x}{d_p} - 1\right)^2 \quad \text{for} \quad 0 \le \frac{x}{d_p} \le \frac{1}{2} \tag{13}$$

$$\varepsilon_f = \varepsilon_f^{bulk} + (\varepsilon_f^{\min} - \varepsilon_f^{bulk})e^{(1/4)-(x/2d_p)}\cos\left(\frac{2\pi x}{d_p c} - \frac{\pi}{c}\right) \quad \text{for} \quad \frac{x}{d_p} \ge \frac{1}{2} \tag{14}$$

where $\varepsilon_f^{bulk} = 0.39$, $\varepsilon_f^{\min} = 0.23$, and $c = 0.816$.

In a fluidized bed the bulk porosity and therefore the porosity close to the wall are both higher than those in a packed bed, especially at higher gas velocities. In addition, the minimum porosity at half a particle diameter distance is altered. Therefore, the minimum porosity should be related to the bulk porosity in the fluidized bed. The following relation is proposed

$$\frac{1-\varepsilon_f^{\min,fl}}{1-\varepsilon_f^{\min,pb}} = \frac{1-\varepsilon_f^{bulk,fl}}{1-\varepsilon_f^{bulk,pb}} \tag{15}$$

where $\varepsilon_f^{\min,pb}$ represents the minimal porosity in a packed bed, $\varepsilon_f^{\min,fl}$ is the minimal porosity in a fluidized bed, $\varepsilon_f^{bulk,pb}$ is the bulk porosity in a packed bed, and $\varepsilon_f^{bulk,fl}$ the bulk porosity in a fluidized bed. The proposed relation assumes that the ratio of the solids bulk porosity and the solids maximal porosity is constant. Although there is no fundamental basis for this correction function, it correctly yields the two limiting cases: if $\varepsilon_f^{bulk,fl} \to \varepsilon_f^{bulk,pb}$, then $\varepsilon_f^{\min,fl} \to \varepsilon_f^{\min,pb}$ and if $\varepsilon_f^{bulk,fl} \to 1$, then $\varepsilon_f^{\min,fl} \to 1$. Assuming that the same values as proposed by Martin[18] (that is, $\varepsilon_f^{\min} = \varepsilon_f^{\min,pb} = 0.23$ and $\varepsilon_f^{bulk} = \varepsilon_f^{bulk,pb} = 0.39$) can be taken, $\varepsilon_f^{\min,fl}$ becomes

$$\varepsilon_f^{\min,fl} = 1 - \frac{0.77}{0.61}(1-\varepsilon_f^{bulk,fl}) \approx 1.26\varepsilon_f^{bulk,fl} - 0.26 \tag{16}$$

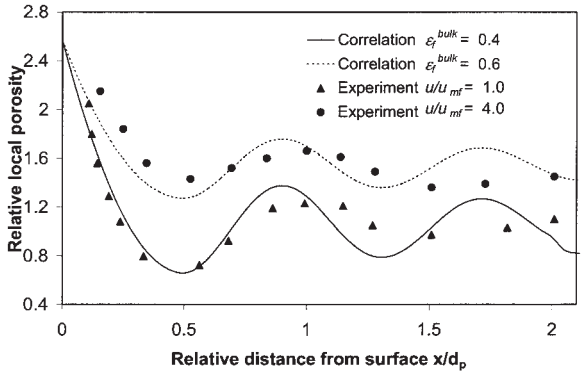

Figure 4. Comparison of the calculated porosity profile (relative to the bulk porosity of a packed bed) near the wall by Martin's modified model for different bulk porosities and experimental data presented by Korolev et al.[15] for different gas velocities.

The modified model of Martin[18] now becomes

$$\varepsilon_f = 1.26\varepsilon_f^{bulk} - 0.26 + 1.26(1-\varepsilon_f^{bulk})\left(\frac{2x}{d_p}-1\right)^2 \quad \text{for} \quad 0 \le \frac{x}{d_p} \le \frac{1}{2}$$

$$\varepsilon_f = \varepsilon_f^{bulk} + 0.26(\varepsilon_f^{bulk}-1)e^{(1/4)-(x/2d_p)}\cos\left(\frac{2\pi x}{d_p c}-\frac{\pi}{c}\right) \quad \text{for} \quad \frac{x}{d_p} \ge \frac{1}{2} \qquad (17)$$

It is assumed that for a fluidized bed, the constant c remains the same as for a packed bed. The relative local porosity distribution near the wall calculated by the proposed modification of Martin's model[18] for different bulk porosities is in good agreement with the experimental data presented by Korolev et al.[15] for different gas velocities, as indicated in Figure 4.

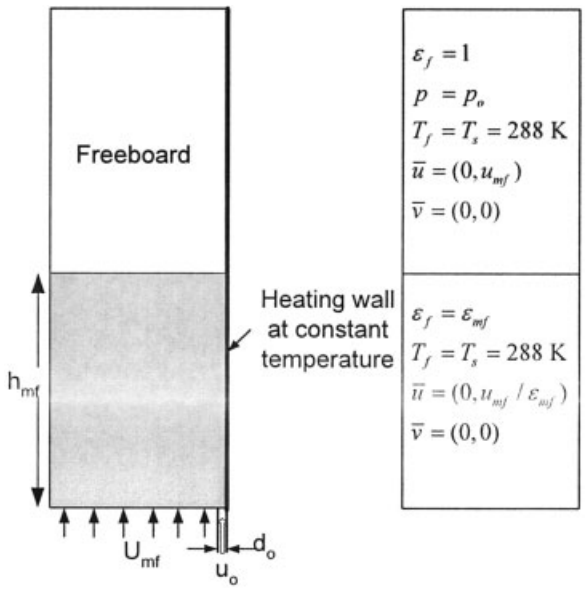

Figure 5. Geometry and the initial conditions used for the simulations.

Table 4. Thermophysical Properties of the Gas and Solids Phases

Property	Gas	Solids	
		Case I	Case II
Diameter of particle (μm)	—	280	460
Density (kg/m^3)	1.2	2600	2660
Specific heat (J kg^{-1} K^{-1})	994	737	737
Heat conductivity (W K^{-1} m^{-1})	0.0257	1.0	1.0
Viscosity (Pa · s)	1.85×10^{-5}	1.0 (CVM)	1.0 (CVM)

Initial and boundary conditions

The initial conditions used for the simulations have been summarized in Figure 5. Because the effective conductivity is a crucial parameter in the thermal energy balance, the porosity profile is used to locally compute the effective conductivity. This model is valid on the scale of a particle diameter from the wall and thus it is imposed only in this range. To determine the sensitivity of the predicted heat-transfer characteristics on the length scale on which the porosity profile is imposed, preliminary calculations were carried out that showed that the solution is independent for a length scale exceeding x^* where $x^* = \max(d_p, 5.0 \times 10^{-4})$. As a boundary condition for the thermal energy balance, a constant wall temperature condition was used for the heated wall and the other walls were assumed adiabatic. For the CVM, no-slip boundary conditions were used for both phases at the confining walls. For the KTGF calculations, the gas velocities were assumed to obey the no-slip condition, whereas the solids were allowed to slip along the wall, following the boundary conditions, given by Sinclair and Jackson,[19] based on a microscopic model for the particle–wall collisions. The local instantaneous heat-transfer coefficient was calculated using

$$h = \frac{\varepsilon_f^* k_f \left|\frac{\partial T_f}{\partial n}\right| + (1-\varepsilon_f^*) k_s \left|\frac{\partial T_s}{\partial n}\right|}{(T_w - T_{bed})} \qquad (18)$$

where T_w represents the wall temperature; T_{bulk} is the bulk temperature of the bed; and k_f and k_s are the microscopic thermal conductivities of the gas and solids phases, respectively.

Numerical Simulations

The model equations have been implemented in the commercial CFD code CFX4.4 (AEA Technology, Harwell, UK). For the evaluation of the convective terms, the third-order total variation diminishing (TVD) scheme min–mod was used. Preliminary calculations showed the existence of a sharp temperature gradient near the heated wall, necessitating the use of a grid-refinement technique to accurately represent the temperature profiles in this thin thermal boundary layer. A grid-independent solution is obtained for a near-wall grid size of 5×10^{-5} m in the direction normal to the wall. The maximum size of the grid in the horizontal direction is 0.0075 m. A uniform

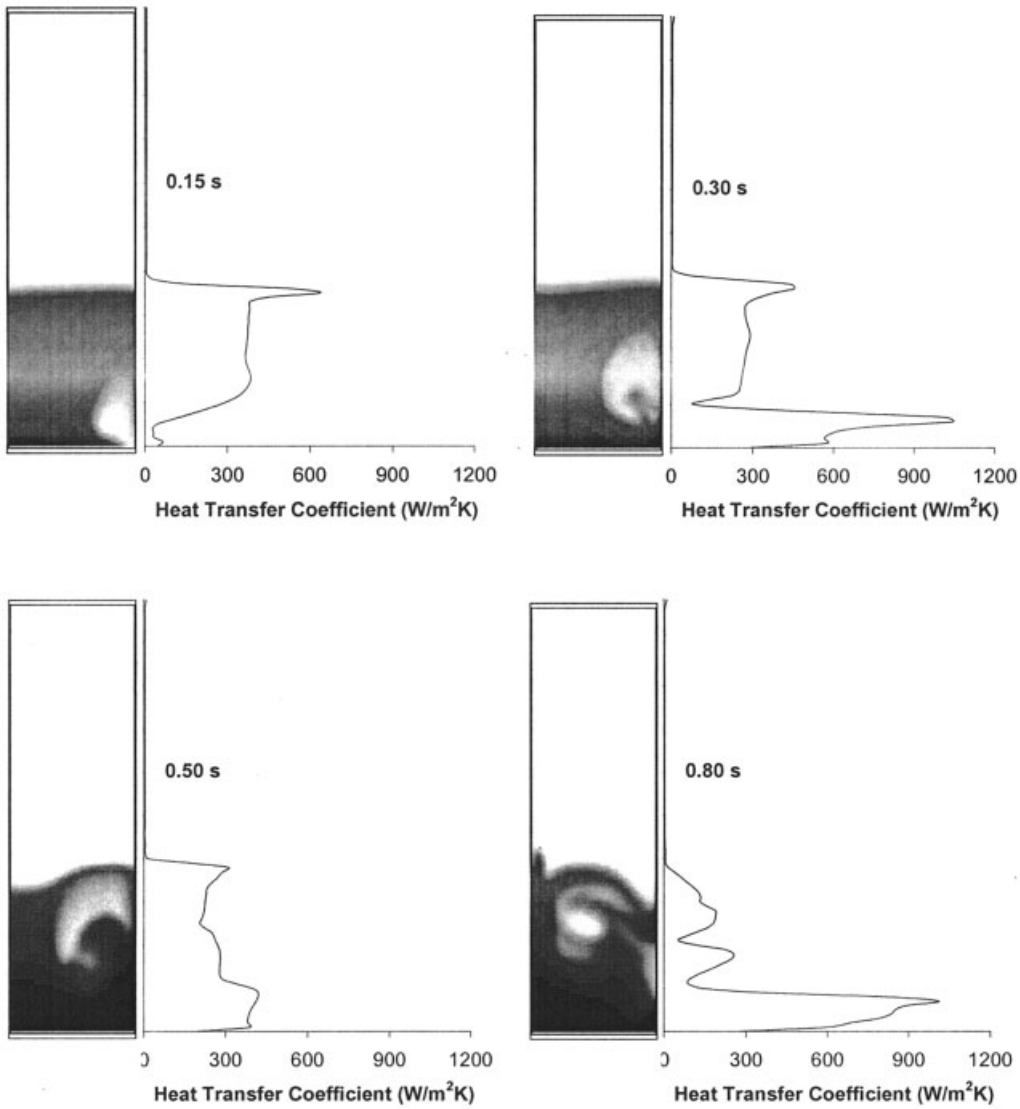

Figure 6. Snapshots of the porosity distribution in the bed and the local and instantaneous heat-transfer coefficient along the heated wall at different moments in time for a pulsating jet with a jet velocity of 5 m/s.

d_p =280 μm; u_{mf} = 0.08 m/s.

grid of 0.01 m has been taken in the vertical direction. The thermophysical data of the gas and solids phase used in the simulations are listed in Table 4.

Computational Results

In bubbling fluidized beds, the solids circulation is caused by the bubbles. The fluid dynamics and heat-transfer characteristics were computed for bubbles injected into the two-dimensional fluidized bed using a pulsating jet and a continuous jet, where the influence of an individual bubble as well as a stream of bubbles on the heat-transfer characteristics was studied. The simulations were carried out with the CVM excluding k_s^{kin} unless otherwise specified.

Pulsating jet operation

With the introduction of air through a jet with a pulse length of 0.25 s and pulse interval of 0.25 s a bubble is formed, which travels along the heated wall of the bed. Figure 6 shows the porosity plots of the bed for a pulsating jet velocity of 5 m/s at different times to illustrate the formation and propagation of the bubble along the wall. The local instantaneous heat-transfer coefficient between the fluid bed and the heated wall predicted by the model is also included in this figure. After the bubble passage, the local heat-transfer coefficient rises very sharply, reaches a maximum, and decreases again. It should be noted that the heat-transfer coefficient is indeed significantly reduced when compared to previous CFD model results, although a detailed validation with the experiments is carried out in the next section.

After the bubble passage, particles from the bulk of the bed rapidly fill the void. During this particle rush, the solids phase is compressed against the wall, resulting in temporary dense packing. However, the particles have only point contacts with the heated wall, and thus the contribution of the direct conductive energy exchange is relatively small. The mechanism of

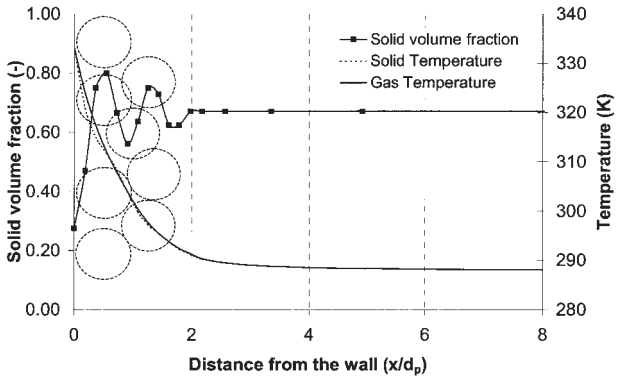

Figure 7. Predicted gas- and solids-phase temperature profiles and solids volume fraction profiles, at 0.1 m above the distributor near the heated wall after 2 s for a pulsating jet velocity of 5 m/s.

d_p =280 μm.

heat transfer between the fluid bed and the wall includes the heat transfer from the heating wall to a thin gas film between the particles close to the wall. The gas in turn transfers the heat to neighboring particles. Botterill and Williams[20] showed with single-particle calculations that indeed a significant amount of heat is transferred to the particulate phase by the surrounding gas.

Figure 7 shows the predicted gas- and solids-phase temperature profiles and the solids-phase volume fraction near the wall, at 0.1 m above the distributor after 2 s. The included schematic representation of the particles shows that the actual resistance of the heat transfer lies in a gas film in the vicinity of the wall with a thickness of approximately two to three particle diameters. By taking into account the porosity distribution near the wall in the effective conductivities, the heat-transfer resistance of the gas film has been modeled. Because the temperature profiles for both phases are almost equal it can be concluded that the resistance of the interphase heat transfer is negligible compared to the overall resistance of the wall-to-bed heat transfer, even at the relatively low particulate phase velocities close to the wall.

Influence of the porosity distribution and convective transport

To demonstrate the significance of accounting for the increased heat-transfer resistance, attributed to the near-wall porosity profile, the heat-transfer coefficients predicted with and without the porosity profile along the wall for 280-μm particles at 0.1 m above the distributor for a pulsating jet of 5 m/s (with pulse length of 0.25 s and pulse interval of 0.25 s) are compared in Figure 8. The predicted results have also been compared with results obtained from the classical penetration theory described by Kuipers et al.,[1] who proposed the following mixture properties:

$$h_{pen} = \sqrt{\frac{k_m(\rho \cdot C_p)_m}{\pi \cdot t}} \tag{19}$$

with $k_m = \varepsilon_f k_f + (1 - \varepsilon_f)k_s$ and $(\rho \cdot C_p)_m = \varepsilon_f \rho_f C_{p,f} + (1 - \varepsilon_f)\rho_s C_{p,s}$.

The penetration theory is valid if the conductive heat-transfer mechanism is dominant in the region near the wall. Note that, because the initial bed temperature was specified as 288 K, whereas the heated wall temperature was instantaneously raised to 333 K, initially infinite wall-to-bed heat-transfer coefficients are predicted.

The importance of the porosity distribution on the predicted local instantaneous heat-transfer coefficient for a bubble rising along a heated wall is clear from Figure 8. Interestingly, the two-fluid simulation without accounting for the porosity distribution predicted lower values for the heat-transfer coefficients than the penetration theory that also uses the bulk porosity to evaluate the effective thermal conductivity. The penetration theory assumes a constant and uniform residence time of the "emulsion packet " at the wall. However, in the wake of the rising bubble the solids circulation locally decreases the residence time of these pockets at the wall, which can explain the observed differences between the predictions of the penetration theory and the two-fluid model without accounting for the local porosity profile near the wall. Furthermore, this indicates that the convective transport mechanism near the wall also plays an important role in the wall-to-bed heat-transfer coefficient.

Experimental validation at lower bed heights

To validate the predicted local instantaneous heat-transfer coefficients with the obtained experimental data, it is necessary to account for the time constant of the sensors using a hypothetical filter with the time constant as that of the heat flux sensors. The resulting filtered heat-transfer coefficient can be calculated by[21]

$$h_{0,k} = e^{-\Delta t/\tau} h_{o,k-1} + (1 - e^{-\Delta t/\tau}) h_{i,k} \tag{20}$$

where $h_{i,k}$ denotes the predicted instantaneous heat-transfer coefficient, Δt is the time interval between two predicted heat-transfer coefficients, τ is the time constant of the sensor (0.02 s), and k is the time level.

Because of the pulsating jet action, bubbles are formed at

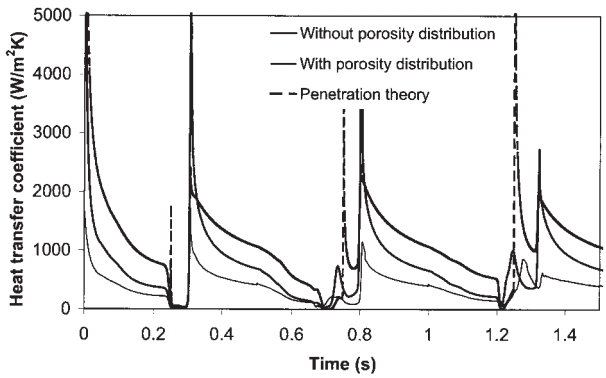

Figure 8. Influence of the incorporation of a porosity distribution on the prediction of the heat-transfer coefficient.

d_p =280 μm; pulsating jet velocity = 5 m/s.

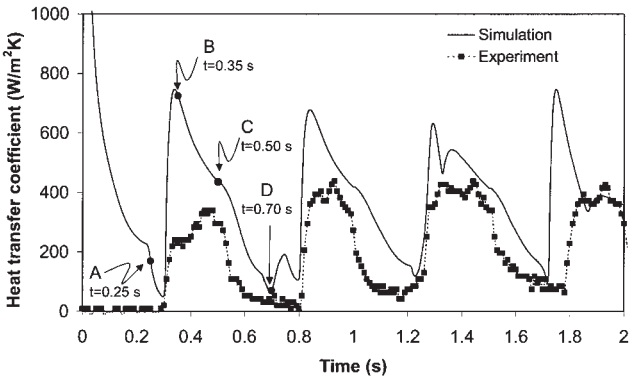

Figure 9. Comparison of the predicted and experimentally determined local instantaneous heat-transfer coefficient at 0.092 m above the distributor as a function of time with experimental data.

d_p = 280 μm; pulsating jet velocity = 5 m/s.

regular time intervals, which subsequently propagate along the heated wall. As mentioned earlier, the predicted heat-transfer coefficient is high in the wake of the bubbles. Figure 9 shows a comparison of the filtered computed and measured heat-transfer coefficients predicted at 0.092 m above the distributor, for a fluidized bed consisting of 280-μm particles operated with a pulsating jet of 5 m/s with a pulse length of 0.25 s and a pulse interval of 0.25 s. A very good agreement between the model predictions and the experiments can be discerned, especially in consideration of the order of magnitude overestimation of the heat-transfer coefficients predicted by previous CFD models that did not account for the local porosity profile near the wall. Again, the predicted high value of the heat-transfer coefficient in the beginning is caused only by the "ideal " start-up conditions specified in the simulations (assuming that the entire bed is initially at room temperature), which does not resemble the experimental initial conditions. In the experiments, the region near the wall was heated up before the measurement of the heat-transfer coefficient began. As also reflected in the experimentally observed heat-transfer coefficients, sometimes in one pulse one maximum is observed and sometimes two maxima are observed. This can be attributed to the formation of multiple bubbles where the passage of the first bubble produces the first peak and the second bubble the second peak.

To clarify the temporal evolution of the local instantaneous heat-transfer coefficient, four time points were selected in Figure 9, ranging from the injection (A) to the eruption of the bubble from the bed (D), for which a snapshot of the solids-phase velocity field including a bubble contour (isoporosity contour of $\varepsilon_f = 0.85$) is plotted in Figure 10. The increase in the heat-transfer coefficient from A (at $t = 0.25$ s) to B (at $t = 0.35$ s) corresponds to the solids rush in the wake of the bubble while passing along the wall. After point B (at $t = 0.35$ s), the rushed solids stay along the wall until point C (at $t = 0.50$ s), after which a new bubble develops at the nozzle.

The bubble passage also influences the solids volume fraction and the gas-phase temperature profile near the wall, given in Figure 11 for the selected points A, B, C, and D indicated in Figure 9. Defining the thermal boundary layer as the region in which the principal temperature gradient is situated, then at A the film thickness is much larger than that at B (see Figure 11b). Because of the solids rush in the wake, the scouring action of solids on the thin gas film is responsible for a decrease in the effective film thickness, thereby increasing the heat-transfer rate.[22] At point C, although the solids volume fraction is equivalent to that at point B, the solids circulation near the sensor is lower because of the movement of the bubble away from sensor. Therefore, the thermal boundary layer becomes "saturated " and the heat-transfer coefficient decreases. At point D, the solids volume fraction is very low, which results in a relatively large film thickness and corresponding low value of the heat-transfer coefficient. The maximum of the predicted

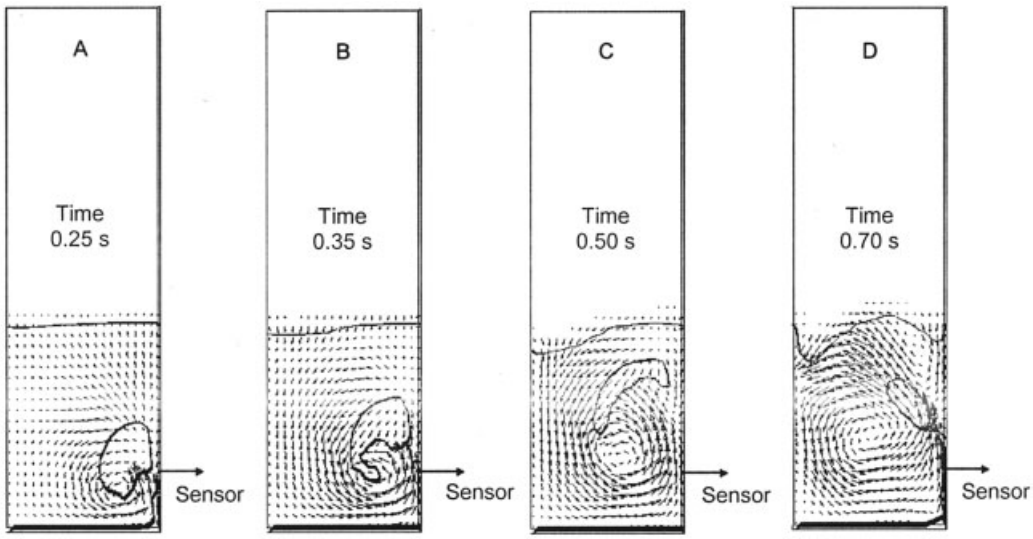

Figure 10. Snapshots of the solids-phase velocity vector field including a bubble contour (isoporosity contour ε_f = 0.85) at different times indicated in Figure 9.

d_p = 280 μm; pulsating jet velocity = 5 m/s.

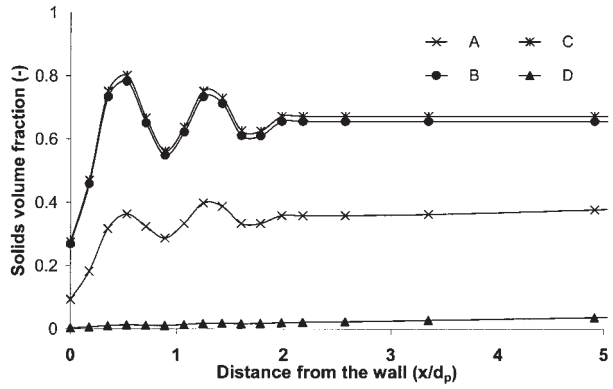

(a)

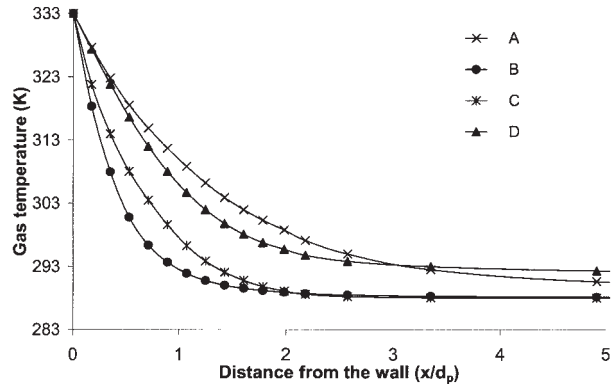

(b)

Figure 11. Comparison of the predicted (a) solids-phase volume fraction and (b) gas-phase temperature profiles for the time points specified by locations A, B, C, and D indicated in Figure 9.

instantaneous heat-transfer coefficient exceeds that of the experimentally determined heat-transfer coefficient probably because of the altered local heat capacity caused by the porosity distribution, which was not taken into account in this model.

Influence of the Jet Velocity. Figure 12 shows an experimental comparison of the predicted heat-transfer coefficient for 280-μm particles at 0.092 m above the distributor for a pulsating jet velocity of 7 and 10 m/s with a pulse length of 0.25 s and a pulse interval of 0.25 s. The model predictions are in very good agreement with the experimental data. With an increase in the jet velocity the bubble size increases, which in turn increases the velocity of the solids rushing into the wake of the bubble, thereby also increasing the heat-transfer coefficient.

Influence of the Particle Size. The particle size is a very important parameter influencing the wall-to-bed heat transfer. The experimentally observed decrease in the heat-transfer coefficient for larger particles is predicted very well by the model that accounts for the local porosity profile near the wall (see Figure 13a) and agrees with the findings of many researchers.[23] For the fluidized bed with larger particles the thickness of the gas film between the first layer of particles and the heated wall is larger, as schematically depicted in Figure 13b, which increases the resistance of the wall-to-bed heat transfer. This effect was accounted for in the model by the porosity distribution along the wall.

Experimental validation at higher bed heights

Figure 14 shows a comparison of the computed and then filtered results with the measured heat-transfer coefficient predicted at 0.259 m above the distributor, for a fluidized bed consisting of 280-μm particles operated with a pulsating jet of 5 m/s with a pulse length of 0.25 s and a pulse interval of 0.25 s. Both the computed and experimentally measured heat-transfer coefficients at 0.259 m above the distributor in the wake of the bubble are lower compared to the heat-transfer coefficient at 0.092 m (see Figure 9). However, the predicted temporal evolution is different when compared to the experimental data. In the simulations, the bubble initially passing along the wall starts to move away from the wall while it rises through the bed, which reduces the wall-to-bed heat-transfer coefficient at higher positions. This behavior is also observed experimentally. However, in the simulations this behavior was overpredicted, which points at inaccuracies in the description of the hydrodynamics near the wall. When the bubble moves away from the wall, the scoring action of the particles is

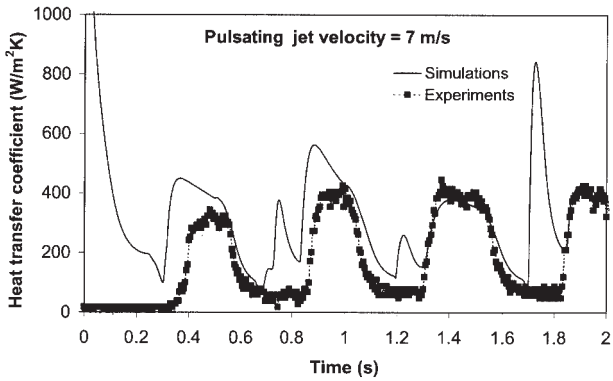

(a)

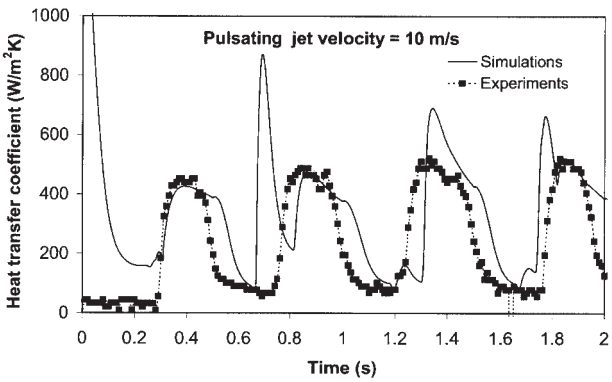

(b)

Figure 12. Comparison of the predicted local instantaneous heat-transfer coefficient at 0.092 m above the distributor as a function of time with experimental data for 280-μm particles and a pulsating jet with a velocity of (a) 7 m/s and (b) 10 m/s.

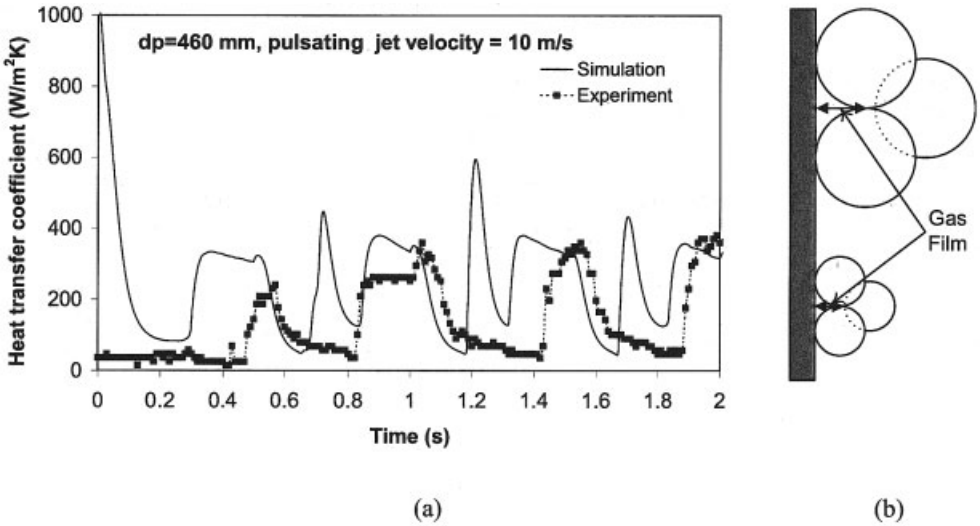

Figure 13. (a) Comparison of the predicted local instantaneous heat-transfer coefficient at 0.092 m above the distributor as a function of time with experimental data for 460-μm particles and a pulsating jet with a velocity of 10 m/s; (b) gas film near the wall for different particle sizes.

reduced, which can be a plausible explanation for the lower value of predicted heat-transfer coefficient at 0.295 m compared to that obtained experimentally. Additional calculations with a free-slip boundary condition showed that indeed the bubble passes exactly along the wall, also at higher bed heights. A partial-slip boundary condition, following the approach proposed by Ding and Gidaspow,[24] was also tried. However, the bubble behavior predicted with this partial-slip boundary condition did not differ significantly from the simulations with the no-slip condition, where the bubble experienced a resistance along the wall and moved away from it.

Continuous jet operation

The dynamic behavior of the wall-to-bed heat-transfer coefficient in the case of operation with a continuous jet is quite similar to that of a pulsating jet, although it is somewhat more chaotic because of the irregular formation of bubbles of nonuniform size. In Figure 15 the predicted local instantaneous heat-transfer coefficient at 0.092 m above the distributor as a function of time for 280 μm particles and a continuous jet with a velocity of 10 m/s is compared with the experimental data, showing good agreement.

The experimental time-averaged heat-transfer coefficient is compared with the predicted time-averaged heat-transfer coefficient as a function of the height along the heated wall for a continuous jet with a velocity of 5 m/s in Figure 16. The measured time-averaged heat-transfer coefficient is calculated by averaging for a period of 60 s, whereas the predicted time-averaged heat-transfer coefficient is obtained by averaging for a period of 2 s because of the required calculation time. The graph shows that the predicted results are in good agreement with the experimental results. Both the simulated and the experimental results show a decrease in the heat-transfer coef-

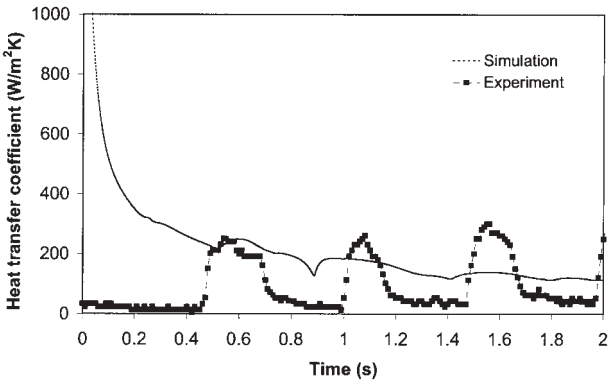

Figure 14. Comparison of the predicted and experimentally determined local instantaneous heat-transfer coefficient at 0.259 m above the distributor as a function of time with experimental data.

d_p = 280 μm; pulsating jet velocity = 5 m/s.

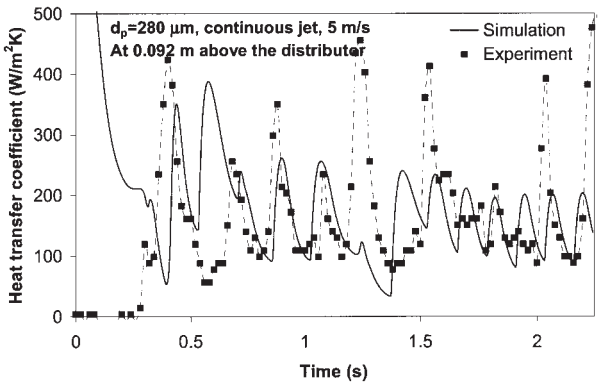

Figure 15. Comparison of the predicted and experimentally determined local instantaneous heat-transfer coefficient at 0.092 m above the distributor as a function of time for 280-μm particles and a continuous jet with a velocity of 10 m/s.

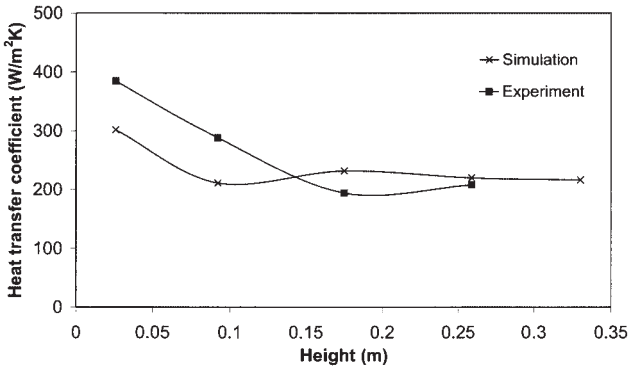

(a)

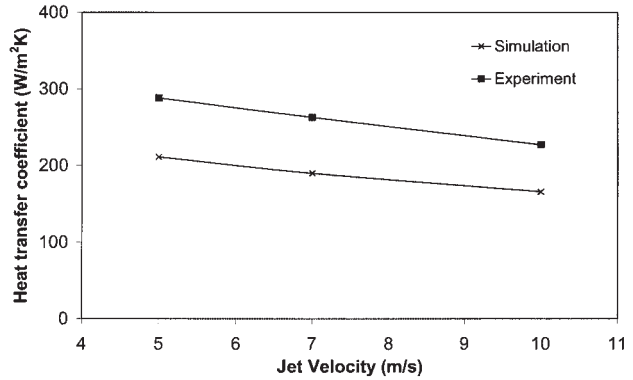

(b)

Figure 16. Comparison of the predicted and experimentally determined time-averaged heat-transfer coefficient for a continuous jet as a function of (a) height in the bed for a jet velocity of 5 m/s; (b) jet velocity at 0.092 m above the bottom distributor.

ficient along the height of the heated wall because the rising bubble moves somewhat away from the wall, which decreases the solids refreshment rate near the wall. This leads to a decrease in the scouring action, resulting in an increase of the gas film thickness. The effect of the jet velocity on the time-averaged heat-transfer coefficient is also shown in Figure 16. At higher jet velocities a slightly lower heat-transfer coefficient was predicted and measured, a consequence of the lower solids volume fraction at the wall caused by the continuous bubble passage resulting in a larger film thickness. The underprediction of the time-averaged heat-transfer coefficient is again caused by the underprediction of the slip along the wall, causing the bubble to move away from the wall in the simulations, more than was observed in the experiments.

Summarizing, the wall-to-bed heat transfer in fluidized beds takes place in close vicinity of the wall and the thickness of the associated "thermal boundary layer " is in the order of magnitude of the size of a particle. Therefore, the porosity distribution near the wall was taken into account by an effective heat conductivity, which substantially improved the predictions. The model predictions showed good agreement with the experimental measurements at lower bed height for both different jet velocities and different particle sizes. At higher bed heights the influence of the bubble passage is underpredicted because the simulations overpredicted the extent to which the bubbles move away from the wall. To further improve the predictions for the heat-transfer coefficients the boundary conditions for the hydrodynamics need careful attention.

Comparison of the KTGF Model with the CVM

Before investigating the influence of the kinetic contribution to the solids-phase effective thermal conductivity using the KTGF model, a comparison is made between the heat-transfer coefficients predicted by the KTGF and the CVM to study the influence of the granular temperature distribution on the correct prediction of the wall-to-bed heat-transfer characteristics. Additional simulations were carried out using the two-fluid model based on the KTGF model together with the thermal energy balance to predict the wall-to-bed heat-transfer coefficient at the heated wall. The simulation details are the same as shown before in Table 4. The particle–particle interactions were assumed inelastic with a restitution coefficient of 0.95. The filtered heat-transfer coefficient predicted at 0.092 m above the distributor (see Figure 17a) by the KTGF without considering

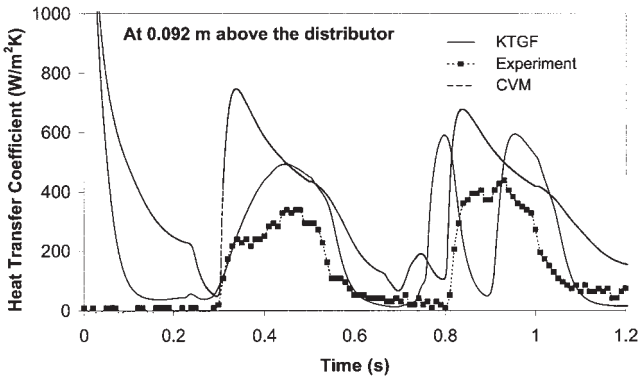

(a)

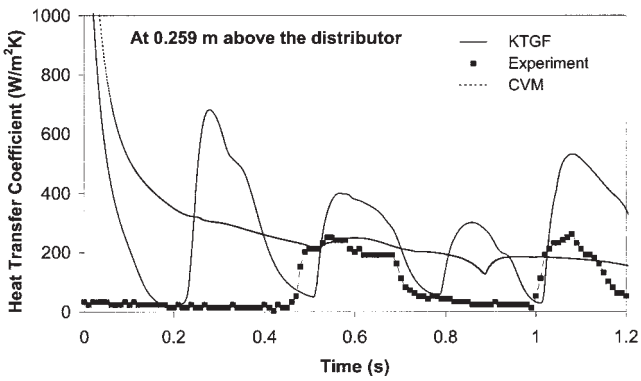

(b)

Figure 17. Experimental comparison of the heat-transfer coefficient predicted by the KTGF and the CVM at (a) 0.092 m and (b) 0.259 m above the distributor.

d_p = 280 μm; pulsating jet velocity = 5 m/s.

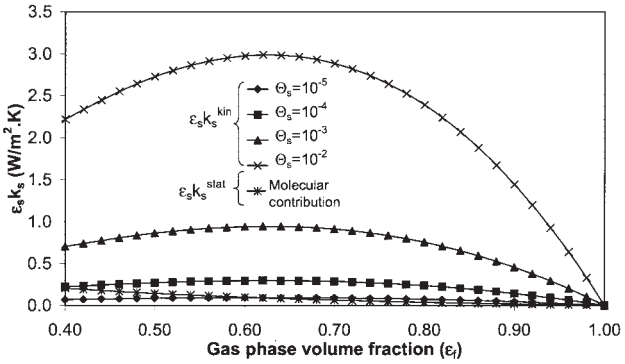

Figure 18. Comparison of the kinetic contribution with the molecular contribution as a function of the gas-phase volume fraction for different granular temperatures.

the kinetic contribution to the effective conductivity is quite similar to the value predicted by the CVM as well as the experimentally obtained heat-transfer coefficient. The additional peak obtained in the temporal evolution predicted by the KTGF is attributed to multiple bubble formation predicted by the KTGF model during one pulse. Similar behavior was also predicted by the CVM, although less pronounced.

At higher bed heights (0.259 m above the distributor), the KTGF model has shown very different behavior compared to the CVM, illustrating the more pronounced influence of the bubble passage, which agrees better with the experimental measurements (see Figure 17b). The boundary conditions used in the KTGF model for the hydrodynamic behavior allow the passage of the bubble along the wall. However, as a consequence of the high shear at the wall, the generation of granular energy is high, thus pushing solids away from the wall. This generates a small gas film near the wall, which evolves into the formation of a bubble moving along the wall. This can be a possible explanation for the difference observed in the prediction by the KTGF model and the experimental measurement.

Influence of the kinetic contribution to the effective heat conductivity

Figure 18 compares the contribution of the solids-phase molecular conductivity and the solids-phase kinetic conductivity to the effective solids-phase thermal conductivity as a function of the gas-phase volume fraction for different granular temperatures. The molecular contribution to the total effective conductivity decreases with an increase in the void fraction because the number of particle contacts decreases. However, because of the turbulent character of the random particle fluctuations, the granular temperature increases in regions of large velocity gradients and low solids volume fractions. For a granular temperature of 10^{-5} m^2/s^2, at high void fractions, the kinetic contribution is predominant, whereas at low void fractions the molecular contribution is predominant. For higher granular temperatures, the kinetic conductivity is predominant for all gas-phase porosities.

With the implementation of the KTGF model, it is possible to evaluate the influence of the kinetic contribution to the effective heat conductivity on the prediction of the heat-transfer coefficient. Figure 19 shows a snapshot of the porosity map of the bed predicted for 280-μm particles for a pulsating jet velocity of 5 m/s (with pulse length of 0.25 s and a pulse interval of 0.25 s). Additionally, axial profiles of the solids-phase volume fraction and granular temperature at the wall and the wall-to-bed heat-transfer coefficient predicted by the KTGF model (accounting for the additional kinetic contribution to the effective solids-phase thermal conductivity) are given. The solids-phase volume fraction profile is again evaluated with the correlation for the porosity distribution near the wall. The predicted granular temperature is higher (in the range of 10^{-1} m^2/s^2) in the wake of the bubble because of the high shear rate, which results in higher heat-transfer coefficients in the wake of the bubble.

Experimental Comparison. Although the influence of the fluctuating motion of the particles on the effective solids-phase thermal conductivity is clear from Figure 19, a comparison of the calculations with experimental data is essential. Figure 20a

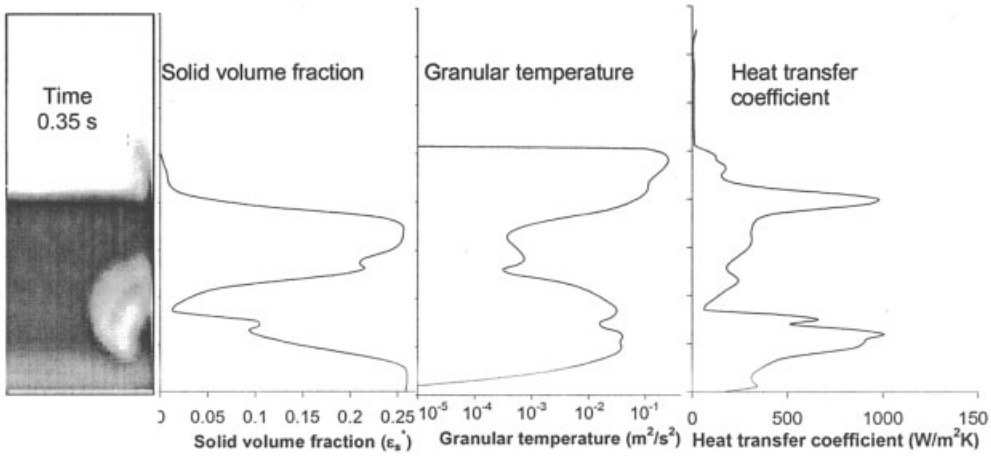

Figure 19. Snapshot of the porosity map with axial profiles of the solids-phase volume fraction (calculated using the porosity profile), granular temperature, and heat-transfer coefficient calculated using the KTGF model.

d_p = 280 μm; pulsating jet velocity = 5 m/s.

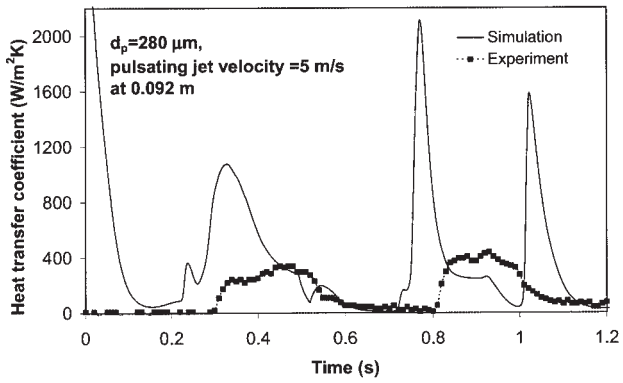

(a)

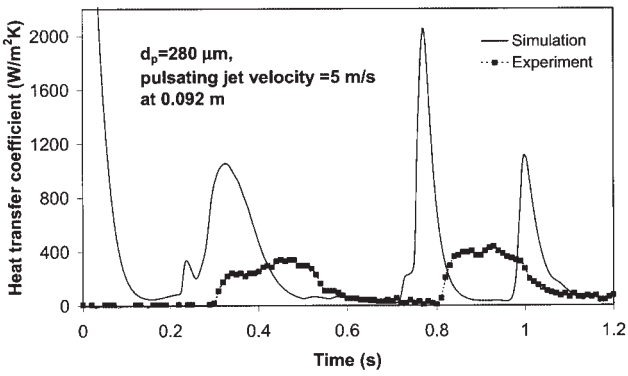

(b)

Figure 20. Experimental comparison of the predicted local instantaneous heat-transfer coefficient at 0.092 m above the distributor as a function of time calculated using the KTGF with (a) accounting for the additional kinetic contribution to the effective solids-phase thermal conductivity; (b) assuming that the effective conductivity equals the kinetic solids conductivity only (following Schmidt and Renz[2]).

d_p = 280 μm; pulsating jet velocity = 5 m/s.

shows a comparison of the predicted heat-transfer coefficient at 0.092 m above the distributor for 280-μm particles predicted by the KTGF model, accounting for the additional kinetic contribution to the effective solids-phase thermal conductivity with experimental results. The heat-transfer coefficient predicted by the model including the additional kinetic contribution to the effective solids-phase thermal conductivity strongly overpredicted the heat-transfer coefficient. During the passage of the bubble the granular temperature is in the order of 10^{-1} m^2/s^2, which leads to a very high solids-phase thermal conductivity, resulting in very high heat-transfer coefficients. With a calculation where only the kinetic contribution to the solids-phase thermal conductivity was taken into account, very similar results were obtained (see Figure 20b), it is demonstrated that the strong overprediction of the wall-to-bed heat-transfer coefficient results from a large overprediction of the kinetic solids-phase thermal conductivity.

Figure 21 shows the radial profile of the granular temperature as a function of the distance from the wall predicted in the wake of the bubble at 0.1 m above the distributor. The granular temperature is very high at the wall as a result of the high shear rate and decreases significantly further away from the wall at a distance of approximately 20 times the particle diameter. Therefore, it is not clear whether we should calculate the kinetic conductivity on the basis of the granular temperature at the wall or at some distance away from the wall. The interpretation of the drastic variation of the granular temperature at such a small length scale is not very clear in terms of particle diffusion. The inelastic particle–wall interactions were accounted for in the calculation of the flux of the granular energy at the wall. However, it is possible that in the dense region an additional dissipation arising from frictional stresses is dominant and needs to be accounted for in the boundary conditions.

Summarizing, the CVM and KTGF models—without the kinetic contribution to the solids-phase conductivity—predicted similar heat-transfer coefficients at lower bed heights, which corresponds well with the experimental findings. However, at higher bed heights, the KTGF model correctly predicted the influence of the bubble passage on the heat-transfer coefficient in contrast to the CVM predictions. The KTGF model,considering an additional kinetic contribution to the effective solids-phase thermal conductivity, strongly overpredicted the heat-transfer coefficient, probably the result of an overprediction of the granular temperature at the wall, which requires further attention.

Conclusions

In fluidized beds, the temperature gradients are very steep in close proximity to the wall and the thickness of the associated "thermal boundary layer " is in the order of magnitude of one particle diameter. Therefore, the porosity distribution near the wall was taken into account by an effective heat conductivity in the thermal energy balance. The computed local instantaneous heat-transfer coefficient for the case of a pulsating jet is in good agreement with the experimentally determined heat-transfer coefficients. The rate of heat transfer depends on the gas film resistance near the wall. In the wake of the bubble the gas film thickness decreases because of the scouring action of the solids, resulting in an increase in the heat-transfer coefficient. The

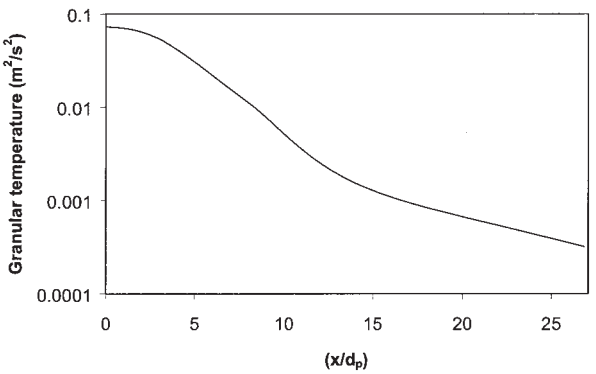

Figure 21. Predicted granular temperature profile near the wall in the wake of the bubble.

0.1 m above the distributor at 0.35 s.

CVM predicts the decrease in the intensity of this scouring action with increasing bed heights caused by the fact that the bubble moves away from the wall, leading to an increased gas film thickness, but overestimates the extent. However, the KTGF model correctly predicts the passage of the bubble along the wall, also showing reasonably good agreement with the experimental measurements at higher bed heights. With an increase in particle size the heat-transfer coefficient decreases as a result of the increase in the gas film thickness and in the case of continuous jet operation, the gas film thickness increases with increasing gas velocity because of the continuous bubble passage that results in a decrease in the heat-transfer coefficient. These experimental observations were correctly and quantitatively predicted by the model.

The KTGF model—accounting for an additional kinetic contribution to the effective solids-phase thermal conductivity—strongly overpredicted the heat-transfer coefficient because of an overprediction of the kinetic solids-phase thermal conductivity. The extremely high predicted granular temperature at the wall could be a possible explanation for this, which requires further research.

Notation

$\boldsymbol{C}$ = fluctuating velocity of the particulate phase, m/s
C_d = drag coefficient
C_p = heat capacity, J kg^{-1} K^{-1}
D_{ij} = strain rate, 1/s^2
d_p = particle diameter, m
e = restitution coefficient for particle–particle collisions
e_w = restitution coefficient for particle–wall collisions
F, r, s = empirical constants for the critical state pressure
f_{corr} = correction factor
G = elastic modulus, Pa
g = gravity constant, m/s^2
g_0 = radial distribution function
h = heat-transfer coefficient, W m^{-2} K^{-1}
H = enthalpy, J/kg
h_{mf} = bed height at minimum fluidization conditions, m
I = current, Ampère
J_h = heat flux, J m^{-1} s^{-1}
k = heat conductivity, J m^{-1} s^{-1} K^{-1}
m = mass of a particle, kg
n = particle number density
Nu = Nusselt number
p = pressure, Pa
P_c = critical state pressure, Pa
Pr = Prandtl number
$\boldsymbol{q}$ = kinetic fluctuation energy flux, kg s^{-3}
R = gas constant, 8.314, J mol^{-1} K^{-1}
Re_p = particle Reynolds number
S = sensor sensitivity, V m^{-2} W^{-1}
T = temperature, K
t = time, s
T_{bed} = average bed temperature, K
T_{wall} = wall temperature, K
u_{mf} = superficial gas velocity at minimum fluidization condition, m/s
$\bar{\boldsymbol{u}}$ = mean gas-phase velocity, m/s
$\bar{\boldsymbol{v}}$ = mean solids-phase velocity, m/s
V = voltage, V
w_b = width of the bed, m
x^* = distance from the wall where a porosity profile is imposed, m

Greek letters

α_p = gas-to-particle heat-transfer coefficient, J m^{-2} K^{-1}
α_s = specularity coefficient
β = interphase momentum transfer coefficient, kg m^{-3} s^{-1}
γ = dissipation rate resulting from inelastic particle–particle collisions, kg m^{-1} s^{-3}
ε = volume fraction
ε_0 = gas-phase porosity in the bulk of a packed bed
ε_{max} = solids volume fraction at packed condition
ε_f^{bulk} = bulk porosity
ε_f^{min}, $\varepsilon_f^{min,pb}$ = minimum value of the near-wall gas porosity for a packed bed
$\varepsilon_f^{min,fl}$ = minimum value of near the wall gas porosity for a fluidized bed (a variable)
Θ = granular temperature, m^2/s^2
κ = conductivity of the granular fluctuating energy, kg m^{-1} s^{-1}
λ = bulk viscosity, kg m^{-1} s^{-1}
μ = shear viscosity, kg m^{-1} s^{-1}
ρ = density, kg/m^3
$\boldsymbol{\tau}$ = shear stress tensor, Pa
τ = time constant of the sensor, s
ϕ = angle of internal friction

Subscripts

f = gas phase
s = solids phase
w = wall

Superscripts

c = collisional contribution
k = kinetic and collisional contribution
f = frictional contribution
kin = kinetic contribution
mol = molecular contribution

Literature Cited

1. Kuipers JAM, Prins W, van Swaaij WPM. Numerical calculation of wall-to-bed heat transfer coefficients in gas-fluidized beds. *AIChE J.* 1992;38:1079-1091.
2. Schmidt A, Renz U. Numerical prediction of heat transfer in fluidized beds by a kinetic theory of granular flows. *Int J Therm Sci.* 2000;39:871-885.
3. Patil DJ, Van Sint Annaland M, Kuipers JAM. Critical comparison of hydrodynamic models for gas–solid fluidized beds: Part I—Bubbling gas–solid fluidized beds operated with a jet. *Chem Eng Sci.* 2005;60:57-72.
4. Ergun S. Fluid flow through packed columns. *Chem Eng Prog.* 1952;48:89-94.
5. Wen YC, Yu YH. Mechanics of fluidization. *Chem Eng Prog Symp Ser.* 1966;62:100-111.
6. Gidaspow D, Ettehadieh B. Fluidization in two-dimensional beds with a jet. 2: Hydrodynamic modeling. *Ind Eng Fundam.* 1983;22:193-201.
7. Nieuwland JJ, Van Sint Annaland M, Kuipers JAM, Van Swaaij WMP. Hydrodynamic modeling of gas/particle flows in riser reactors. *AIChE J.* 1996;42:1569-1582.
8. Srivastava A, Sundaresan S. Analysis of a frictional-kinetic model for gas-particle flow. *Powder Technol.* 2003;129:72-85.
9. Gunn DJ. Transfer of heat or mass to particles in fixed and fluidised beds. *Int J Heat Mass Transfer.* 1978;21:467-476.
10. Zehner P, Schlünder EU. Wärmeleitfähigkeit von schüttingen bei mässigen Temperaturen. *Chem Ing Tech.* 1970;42:933-941.
11. Syamlal M, Gidaspow D. Hydrodynamics of fluidization: Prediction of wall-to-bed heat transfer coefficients. *AIChE J.* 1985;31:127-135.
12. Natarajan VVR, Hunt ML. Kinetic theory analysis of heat transfer in granular flows. *Int J Heat Mass Transfer.* 1998;41:1929-1944.
13. Hunt ML. Discrete element simulations for granular material flows: Effective thermal conductivity and self diffusivity. *Int J Heat Mass Transfer.* 1997;40:3059-3068.
14. Chapman S, Cowling TG. *The Mathematical Theory of Non-uniform Gases*. 3rd Edition. Cambridge, UK: Cambridge Univ. Press; 1970.
15. Korolev VN, Syromyatnikov NY, Tolmachev EM. Structure of a fixed

bed of granular material near an immersed surface (wall). *J Eng Phys.* 1971;21:1475-1478.
16. Kubie J, Broughton J. A model of heat transfer in gas fluidized beds. *Int J Heat Mass Transfer.* 1975;18:289-299.
17. Benenati RF, Brosilow CB. Void fraction distribution in beds of spheres. *AIChE J.* 1962;8:359-361.
18. Martin H. Low Péclet number particle-to-fluid heat and mass transfer in packed beds. *Chem Eng Sci.* 1978;33:913-919.
19. Sinclair JL, Jackson R. Gas-particle flow in a vertical pipe with particle–particle interactions. *AIChE J.* 1989;35:1473.
20. Botterill JSM, Williams JR. The mechanism of heat transfer to gas-fluidized beds. *Trans IChemE.* 1963;41:217.
21. Roffel B, Chin P. Computer control in the process industries. Chelsea, MI: Lewis Publishers; 1987.
22. Kilkis B. Computer aided analysis of fluidized bed to external wall local heat transfer. *Chem Eng J.* 1991;46:47-60.
23. Molerus O, Burschka A, Dietz S. Particle migration at solid surfaces and heat transfer in bubbling fluidized beds. I: Particle migration measurement systems. *Chem Eng Sci.* 1995;0:871-877.
24. Ding J, Gidaspow D. A bubbling fluidization model using theory of granular flow. *AIChE J.* 1990;36:523-538.
25. Bouillard JX, Lyczkowski RW, Gidaspow D. Porosity distributions in the fluidized bed with the immersed obstacle. *AIChE J.* 1989;35:908-922.
26. Grace JR. The viscosity of fluidized beds. *Can J Chem Eng.* 1970;48: 30-33.
27. Schügerl K, Merz M, Fetting F. Rheologische Eigenschaften von gasdurchströmten Fleissbettsystemen. *Chem Eng Sci.* 1961;15:1-38.
28. Ocone R, Sundaresan S, Jackson R. Gas-particle flow in a duct of arbitrary inclination with particle–particle interactions. *AIChE J.* 1993; 39:1261-1271.

Manuscript received Jan. 6, 2005, and revision received Apr. 29, 2005